# Chapter 5

# $Fe_3O_4$ mesoporous nanoparticles

# Chapter 5: $Fe_3O_4$ mesoporous nanoparticles

## 5.1. Introduction

Iron oxide magnetic nanoparticles (IONPs), *viz.* $Fe_3O_4$ and $\gamma$-$Fe_2O_3$, have shown great potential as promising candidates for MFH and PTT based cancer treatments. In addition, mesoporous hybrid MNPs created with a porous silica shell and a magnetic core significantly benefit the cancer therapy, i.e. higher chemotherapeutic drug loading, magnetically controlled delivery and combined toxic hyperthermia and temperature sensitive drug release [188], [189]. However, the presence of silica shell significantly deteriorates the magnetic properties of the hybrid system. A porous magnetic core particle itself could alleviate such issue. *Shi et al*. [190] could synthesize such mesoporous $CoFe_2O_4$ nanoparticles through a facile solvothermal method which showed an improved drug loading capacity, making them suitable for drug delivery application. *Xin et al.* [191] synthesized amine-functionalized $Fe_3O_4$ nanoparticles which showed highly efficient removal of heavy metal ions. *Cheng et al.* [75] examined and demonstrated the importance of the choice of solvent and reaction conditions in obtaining the mesoporous magnetic properties of the nanoparticles.

Here, the exploration of the heating behaviour of mesoporous MNPs was of interest when exposed under an AMF and NIR radiation for MFH and PTT applications, respectively, for cancer cell destruction. This work possesses a variety of novel components under one umbrella wherein highly mono-dispersed mesoporous $Fe_3O_4$ NPs was designed through solvothermal process (*chapter 2, sec. 2.2.3*). The heating performance of the $Fe_3O_4$ mesoporous NPs was demonstrated by exposing them to AMF during MFH and NIR irradiation for PTT. While the sample depicted effective heating during MFH, a notable temperature rise was observed under NIR irradiation of low power density. The structural

and magnetic properties of the sample were thoroughly studied. Its photoluminescence study facilitated the realization of the high heating performance of the sample during PTT.

## 5.2. Results and discussion

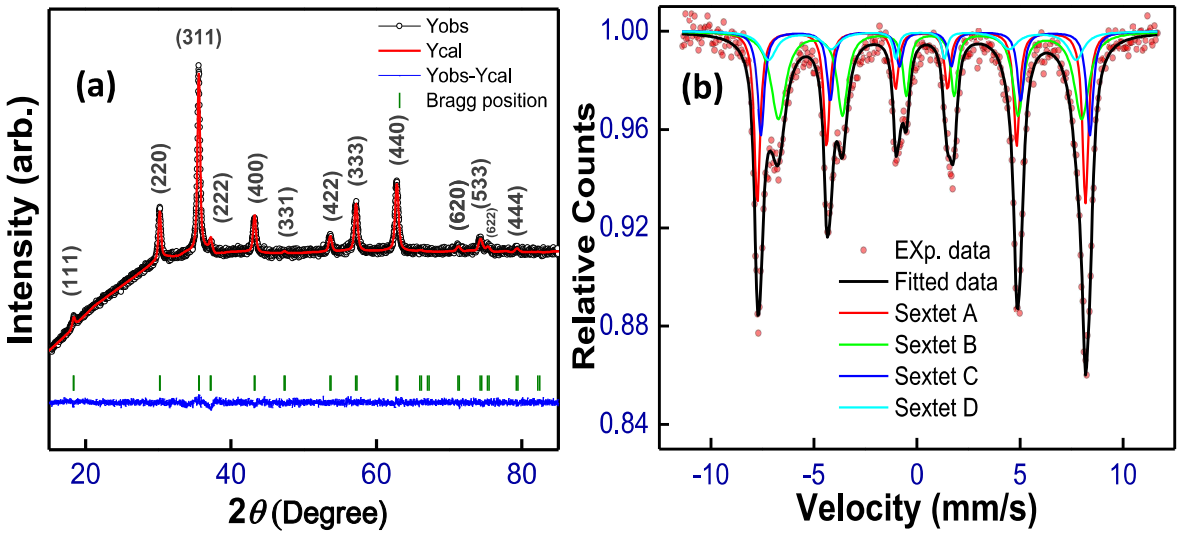


*Figure 5. 1: (a) Rietveld refined XRD pattern and (b) room temperature Mössbauer spectrum of powder sample.*

*Figure 5.1a* shows the Rietveld refined XRD pattern of the sample obtained at room temperature. The pattern suggests the formation of single-phase material with the cubic crystal structure (space group *Fd-3m*, No. 227). Within the limit of the resolution, no impurity phase was detected in the XRD pattern. To model the XRD peak profile, the Thompson-Cox-Hastings pseudo-Voigt function was utilized. The factors relating to the reliability of fit, i.e. $R_{wp}$, $R_e$ and $Chi^2$, were converged to 16.6, 15.6 and 1.13, respectively, after the refinement. The material's crystal lattice parameter (a) obtained as 8.37 Å after the refinement, was smaller than that of bulk $Fe_3O_4$ (a = 8.39 Å). Such a decrease in the lattice parameter of $Fe_3O_4$ has been observed previously and was attributed to the oxidation of a fraction of $Fe^{2+}$ to $Fe^{3+}$ ions at the surface [192], [193]. The crystallite size of the sample was obtained to be ~23 nm.

Further, Mössbauer spectroscopy could provide an insight into the stoichiometric chemical composition of the sample [194].

*Figure 5.1b* shows the Mössbauer spectrum of the sample acquired at room temperature. Interestingly the spectrum depicted a well resolved magnetically split absorption lines, suggesting a magnetically ordered state within the sample. Such an observation is a typical characteristic of a ferri-magnetic material [169]. The spectrum also suggests a higher blocking temperature of the magnetic moments than 300 K. With Gaussian profile, the best fitting of the spectrum was achieved with four sub-spectra, which could be assigned to the iron ions having different local environments. The hyperfine parameters such as hyperfine field ($H_f$) and isomer shift (IS) experienced by an iron nucleus are sensitive to its local environment and can distinguish Fe nucleus with different coordination environments. *Table 5.1* represents the parameter extracted from the Mössbauer spectrum of the powder sample.

*Table 5. 1: Parameters obtained from room temperature Mössbauer spectrum of powder sample.*

| *Site* | *Hyperfine field ($H_f$), T ± 0.01* | *Isomer shift (δ) mm/s ± 0.01* | *Quadruple splitting (Δ) mm/s ± 0.02* | *Outer line width (Γ) mm/s* | *Relative area (RA) ± 0.03%* | *$X^2$* |
|---|---|---|---|---|---|---|
| *Sextet A* | 49.40 | 0.219 | -0.013 | *0.348* | *27.5* | |
| *Sextet B* | 45.65 | 0.640 | -0.009 | *0.870* | *40.3* | *1.13* |
| *Sextet C* | 49.50 | 0.411 | -0.005 | *0.390* | *21.5* | |
| *Sextet D* | 46.26 | 0.207 | 0.107 | *0.886* | *10.7* | |

The high spin $Fe^{3+}$ ionic state is always characterised by a lower IS value than its +2 ionic state counterpart [195]. Moreover, this value is observed to be relatively higher for $Fe^{3+}$ ions positioned at the octahedral site in $Fe_3O_4$ compared to $Fe^{3+}$ in the tetrahedral position [195], [196]. The sub-spectrum, sextet A, with the smallest IS value of 0.219 $mms^{-1}$ could be attributed to $Fe^{3+}$ positioned at the tetrahedral site. The corresponding $H_f$ value for this subset was 49.40, which is close to the value of bulk $Fe_3O_4$. The sextet B exhibited a moderate IS value (0.640 $mms^{-1}$), suggesting a combined involvement of $Fe^{2+}$ and $Fe^{3+}$ ions for this sub-spectrum. Thus, it could be assigned to $Fe^{2.5+}$ ionic state at the octahedral site. The intermediate $Fe^{2.5+}$ ionic state at octahedral position could arise from the hopping of electrons between $Fe^{2+}$ and $Fe^{3+}$ ions located at these positions, which is observed above Verwey transition temperature [17], [194]. The hyperfine field value corresponding to this sub-spectrum was 45.65 T, which is lower than sextet A and is in line with the previous reports [17], [193], [197]. The sextet C exhibited an $H_f$ value of 49.50 T and an IS value of 0.411 $mms^{-1}$, which could be assigned to $Fe^{3+}$ in the octahedral position. Further, a wider outer line width could be observed for sextet B than sextets A and C. It indicates a distribution of hyperfine field which might have existed due to different coordination environments of $Fe^{2+}$ and $Fe^{3+}$ at the octahedral position. The fourth sub-spectrum, i.e. sextet D could be due to the $Fe^{3+}$ species present at the surface of the material [197]. It has an $H_f$ value of 46.26 T, which is smaller than the $H_f$ value obtained for $Fe^{3+}$ species from the core atoms. Again, a relatively wider outer line width for sextet D suggests a distribution of hyperfine field, which might have existed due to the broken symmetry of surface atoms leading to dissimilarity in the local coordination environments. Nevertheless, it exhibited a significant quadruple splitting which might be associated with broken symmetry at surface atoms. Finally, the total fraction of $Fe^{2+}$ ions in the sample was obtained as 0.28. This value is deviating from the stoichiometric

values for magnetite which is 0.33. Several authors have observed such deviation from the stoichiometric structure due to defects in nano-metric magnetic samples [17], [194]. Nevertheless, a more precise interpretation could be obtained at a lower temperature, but with the limitation of the instrument, it is not possible to carry out such experiments.

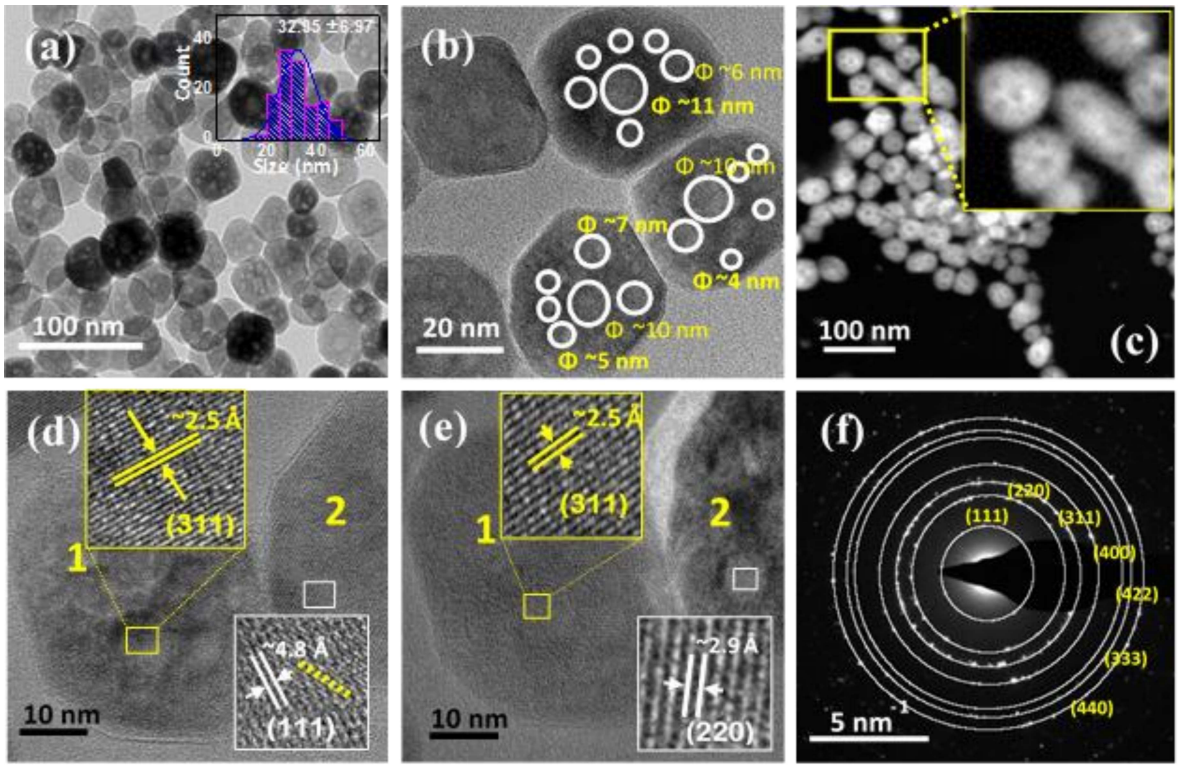


*Figure 5. 2: (a) Bright-field TEM image (the insets show the size distribution profile), (b) high-magnification TEM image marked with the diameter, (c) HAADF-TEM image, (d) & (e) high-resolution TEM images and (b) SAED pattern of the meso-porous $Fe_3O_4$ sample.*

Transmission electron microscopy has provided some fascinating insight into the particles' morphology. The bright-field (BF) TEM image shown in *Figure 5.2a* suggests that the particles were nearly spherical with an average size of ~32 nm (S.D. ~7 nm). A careful look at the images during the BF TEM indicated the formation of nanopores in the particles. At higher magnification, as depicted by *Figure 5.2b*, the nanopores could be spotted easily.

As calculated with the help of Image J software, the size of these pores was found to be ranging from ~4 to 11 nm.

These nanopores were realized well with TEM in HAADF mode, where the inverse contrast (dark) could be ascribed to the pores in the particles (*Figure 5.2c*). The figures depicted a dip in the energy counts at darker positions. Thus, these darker portions are essentially the pores present in the particle. *Figure 5.2(d & e)* show the high-resolution TEM images of two particles, marked as 1 and 2. In *Figure 5.2d*, the electron beam was focused on particle 1, which showed the lattice fringes with an inter-planar spacing of ~2.5 Å and matched the plane (311). At this focus, particle 2 showed lattice fringes over the surface, and any depression was not observed on its surface. The lattice fringes observed for particle 2 had an inter-planar spacing of ~4.8 Å, which corresponds to the (111) plane of $Fe_3O_4$. However, at different places relatively closer lattice fringes could be observed with different orientations. One such position has been highlighted with a white square shown in *Figure 5.2d*. With a variation in focus pores can be observe in particle 2, as shown in *Figure 5.2e*. The lattice fringes corresponding to the pores had different orientation than observed for the same particle in *Figure 5.2d*. The lattice fringes had an inter-planar spacing of ~2.9 Å corresponding to the plane (220) of $Fe_3O_4$. Also, the surface of particle 2 showed the same crystal planes as that of the pores. However, the depression observed on the surface of particle 1, in *Figure 5.2d*, vanished in this case. Nevertheless, the observed lattice fringes in particle 1 still had the same orientation and inter-planar spacing as observed before. The SAED pattern given in *Figure 5.2f* suggests the formation of a single-phase cubic structure, thus validating the XRD result. Further, it was strengthened by taking a line profiling across a single particle as shown in *Figure 5.3*.

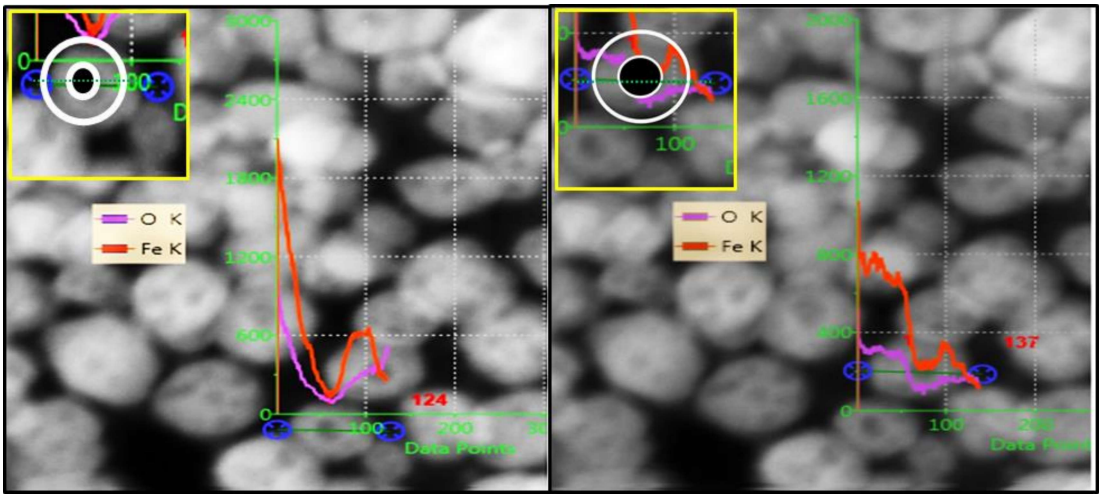


*Figure 5. 3: HAADF-STEM line profile of mesoporous $Fe_3O_4$ nanoparticles.*

The mesoporous $Fe_3O_4$ nanoparticles was synthesized in a solvent of composition 75% DEG and 25% EG. In addition, PVP was used as a surfactant to control the particles' size. The boiling point of DEG is 244 °C, while EG boils at 197 °C. Detailed information on the synthesis process is provided in chapter 2 (*sec.2.2.3*). As described, the sample was prepared at 200 °C, higher than the boiling temperature of EG but lower than that of DEG. At this temperature, the EG molecules (in DEG+EG) attached with the $Fe_3O_4$ nuclei or some other intermediate complexes formed during heating in span to reach the synthesis temperature (200 °C) might have escaped from the solvent through the evaporation, creating pores in the particles. To confirm this hypothesis, a series of experiments was performed varying the contents of the solvent used during synthesis.

*Figure 5.4* shows the schematic representation of the details of the various synthesis process undertaken. The path marked with 1 is discussed above, which leads to mesoporous particles' formation. The synthesis process marked with 2 was carried out in the same solvent, i.e. 75% DEG and 25% EG, but without PVP polymer surfactant. Clearly, the formation of

pores can be observed in the particles following this synthesis route also (*Figure 5.5a and b*), which supports our hypothesis.

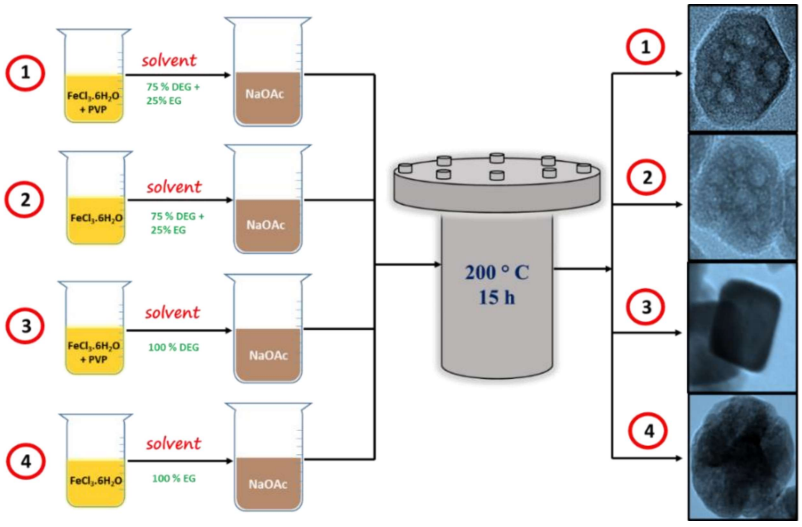


*Figure 5. 4: Schematic representation of synthesis process.*

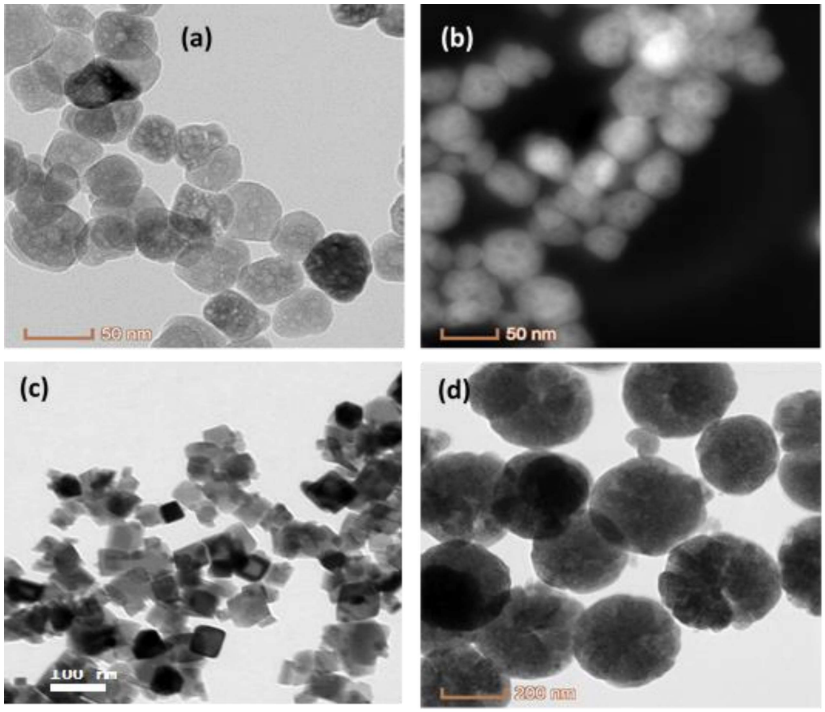


*Figure 5. 5: (a &b) Bright-field and HAADF-TEM images of the sample obtained in solvent consisting of 75% DEG and 25% EG (route 2), (c) bright-field TEM images of the sample obtained in solvent 100% DEG (route 3) and (d) 100% EG (route 4).*

However, an increase in particles' size was evident as PVP was not present in this case to restrict particle growth. The particles showed a mean size of ~43 nm (S.D. ~7.5 nm), which was 30% higher than that obtained when PVP was used. In process '3', only DEG was used as the solvent and PVP as surfactant. The particles obtained through this process showed faceted like morphology and no pores were observed. The particles had a mean size of ~61 nm (S.D. ~10 nm). Finally, only EG was used as the solvent for the synthesis (path 4). The particles obtained through this path were spherical with an average size of ~320 nm (S.D. ~18 nm). Thus, these experiments endorse our assumption that the lower boiling EG in 75% DEG and 25% EG was responsible for forming a porous structure. Moreover, using anhydrous salt of $FeCl_3$ to prepare the sample through route 1 also resulted in the formation of mesoporous nanostructure (*Figure 5.6*). The result further strengthens our conclusion. *Cheng et al.* [75] observed the formation of porous iron oxide nanoparticles when employed 1,2-propylene glycol instead of EG as the solvent in a solvothermal reaction.

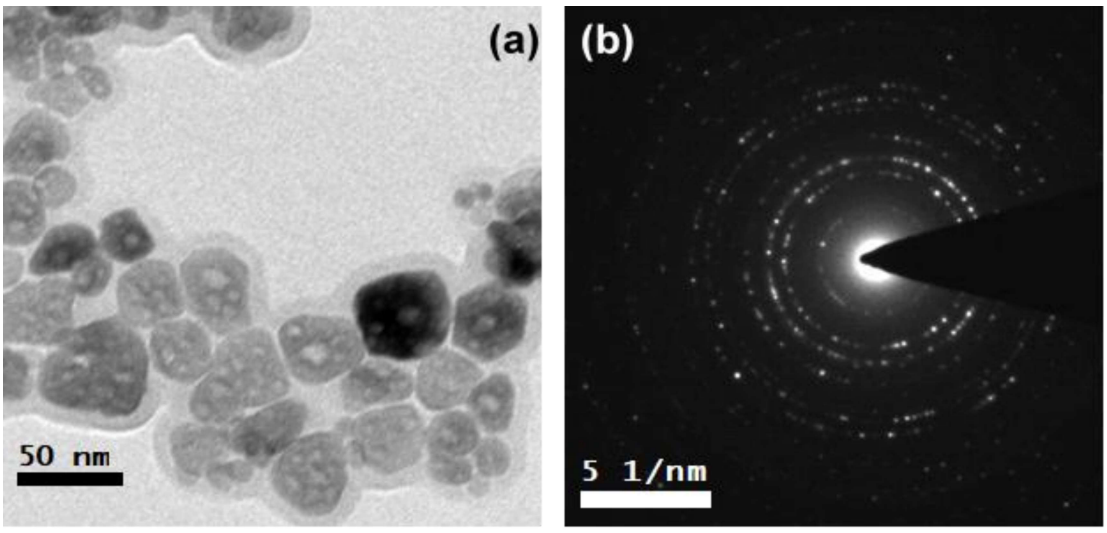


*Figure 5. 6: (a) Bright-filed TEM image and (b) SAED pattern of the sample obtained using anhydrous $FeCl_3$ through route 1.*

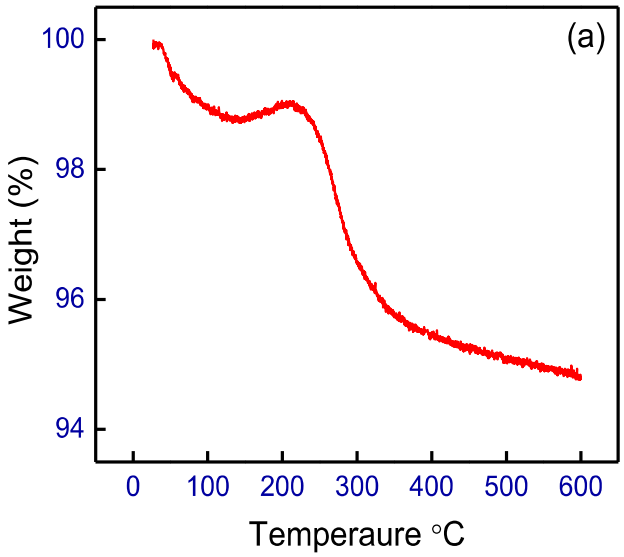


*Figure 5. 7: (a) TGA curve, and (b) FT-IR spectrum of meso-porous $Fe_3O_4$ nanoparticles.*

The thermo-gravimetric analysis (TGA) performed in temperature range of 30 – 600 °C assessed the amount of adsorbed chemical species by the MNPs. The TGA curve (*Figure 5.7*) revealed a total weight loss of around 5% during the heating up to 600 °C. The initial weight drops up to 150 °C can be linked to the evaporation of physically adsorbed water molecule and low boiling organic complexes attached to the surface of MNPs [172], [173]. A slight increase in mass starting just above 140 °C and up to almost 220 °C can be assigned to the oxidation of $Fe_3O_4$ to $\gamma$-$Fe_2O_3$. In temperature range 220 to 350 °C a sharp decrease in weight was observed which could be due to the chemical decomposition of chemically adsorbed organic species. Above 350 °C a slight drop in weight up to the measuring temperature of 600 °C might be associated with the decomposition of attached PVP molecule [173].

For the magnetic properties evaluation of the sample at room temperature (300 K) and low temperature (5 K), the hysteresis loops were recorded up to ± 50 kOe applied magnetic field and are represented in *Figure 5.8a*. Fascinatingly, the curve displayed an early

saturation characteristic with a finite hysteresis at both temperatures. The magnetic parameters extracted from the hysteresis curve *viz.*, saturation magnetization ($M_S$), coercive field ($H_C$) and remanent magnetization ($M_r$) are presented in *Table 5.2*. The sample exhibited saturation magnetization ($M_S$) of ~83 and 91.5 emu/g at 300 and 5 K, respectively. The values are very close to that of the bulk $Fe_3O_4$, which directs to the synthesis of high quality magnetic nanoparticles through the process employed [197]. At room temperature, the material depicted a typical soft ferri-magnetic nature with a $H_C$ of ~ 45 Oe, which increased to ~218 Oe at 5 K. The ferri-magnetic behaviour of the sample was earlier confirmed through Mössbauer spectroscopy.

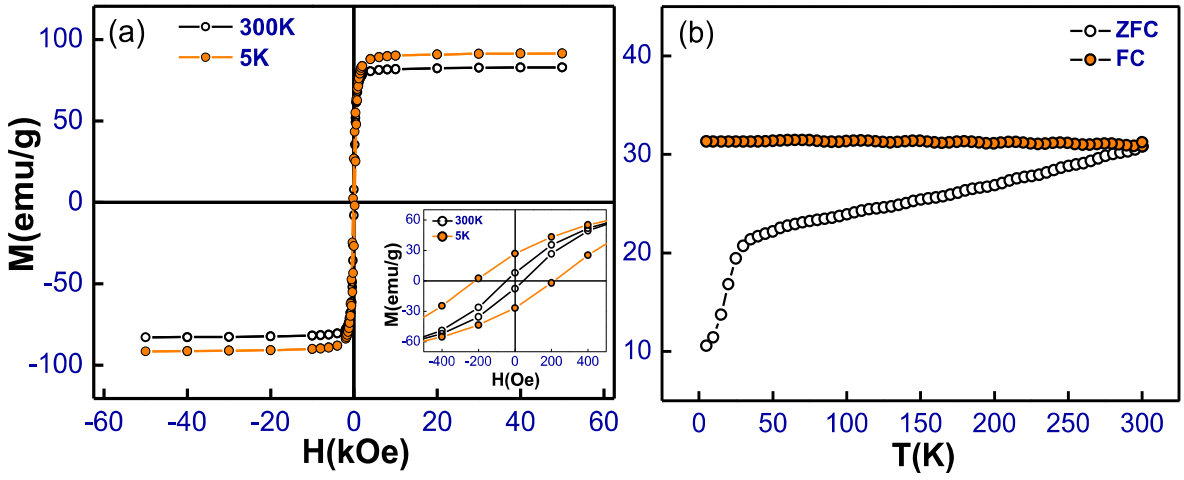


*Figure 5. 8: (a) Magnetisation vs. field loops at 300 and 5 K and (b) temperature dependent (5 – 300 K) magnetic behaviour (ZFC-FC) of meso-porous $Fe_3O_4$.*

*Table 5. 2: Magnetic parameters obtained from M-H loops of mesoporous Fe3O4 measured at 300 and 5 K.*

| Temperature (K) | $M_s$ (90 kOe) (emu/g) | $M_r$ (emu/g) | $M_r/M_s$ | $H_c$ (Oe) |
|---|---|---|---|---|
| 300 | 83 | 7.9 | 0.095 | 45 |
| 5 | 91.5 | 26.8 | 0.293 | 218 |

Further, the temperature-dependent magnetization curves (ZFC and FC) measured from 5 to 300 K with an excitation field of 250 Oe are shown in *Figure 5.8b*. The sample depicted an irreversible behaviour in the entire range of measurement temperature, suggesting that all the particles were essentially in the blocked state [169]. Since the applied excitation field was 250 Oe, the irreversibility or the bifurcation between the ZFC and FC curves suggests that a high anisotropy barrier existed in the sample and the magnetic moments could not align completely in the field direction at the excitation amplitude. For the magnetic hyperthermia study an AMF of amplitude 170 Oe was applied, which is still on the lower side; thus, better heating than reported could be achieved with a higher amplitude AMF. Interestingly, the FC magnetization displayed a temperature-independent behaviour and was flat in the entire temperature range. Such observation directs to a material with strong magnetic inter-particle and dipole-dipole interaction [169].

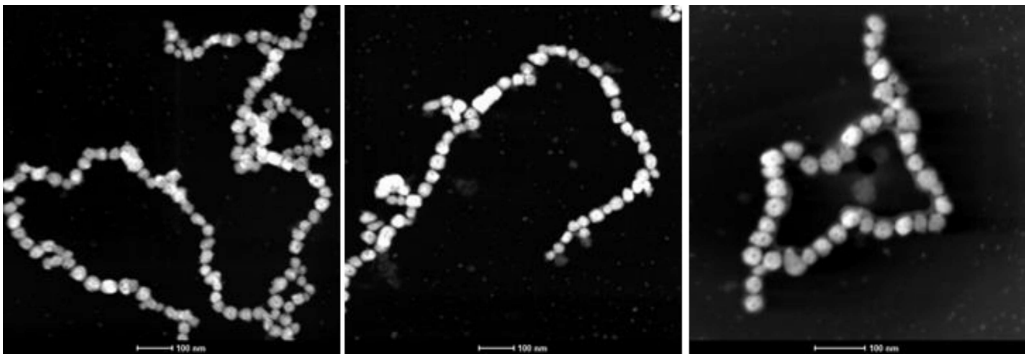

*Figure 5. 9: HAADF-TEM images of meso-porous $Fe_3O_4$ (obtained from route 1) displaying the chain formation.*

The chain-like assembly of the nanoparticles was also observed at various positions in TEM (*Figure 5.9*), and thus a strong inter-particle interaction is justified in the FC magnetization curve. Such magnetic interactions contribute to step up the overall anisotropy energy and would modify the heating performance of the material during MFH [46]. In

addition, a change in slope of the ZFC curve could be observed below ~35 K, associated with the Verwey transition of $Fe_3O_4$. Though the Verwey transition in bulk $Fe_3O_4$ is observed ~120 K, it is observed at lower temperatures in $Fe_3O_4$ having particles' size < 50 nm [17]. Nevertheless, such a transition vanishes in $Fe_3O_4$ with particles having size smaller than 10 nm.

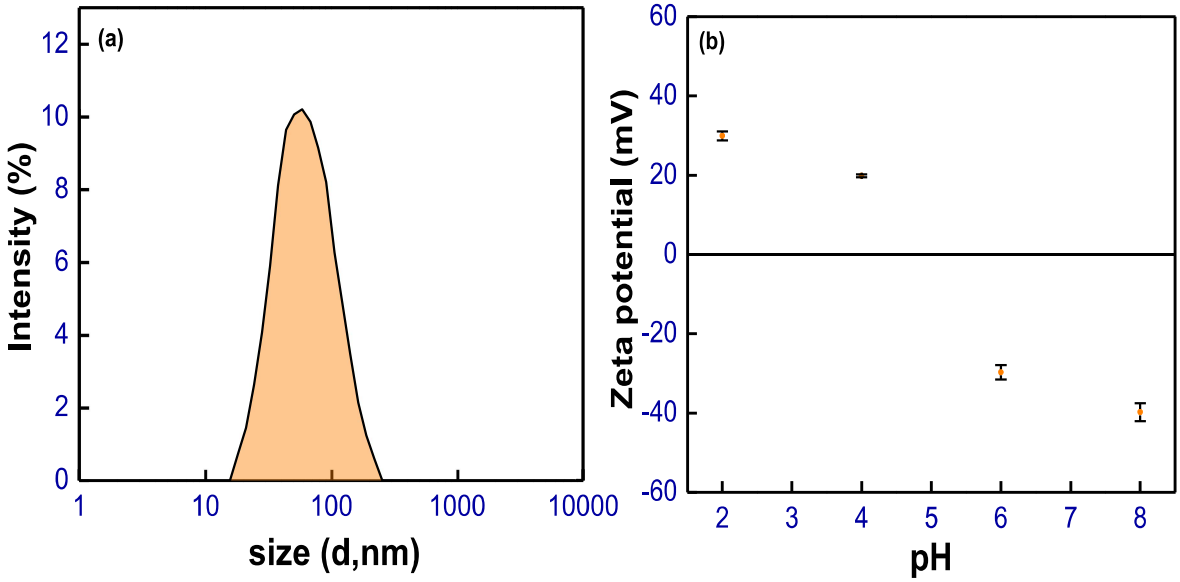


*Figure 5. 10: (a) DLS – hydrodynamic size profile and (b) pH dependent zeta-potential of particles in aqueous ferrofluid.*

The aqueous ferrofluid showed good stability as observed from the zeta potential (ζ) measurement. The mean ζ values were quantified as 29.93 ± 1.09, 19.86 ± 0.32, -29.73 ± 1.85 and -41.7 ± 2.27 at 2, 4, 6 and 8 pH values, respectively (*Figure 5.10b*). The dynamic light scattering plot (*Figure 5.10a*) depicted a uni-modal distribution of hydrodynamic size ($D_h$) for the particles dispersed in the aqueous medium. The mean $D_h$ value was observed to be 73 ± 1.31, which was higher than the particle's size observed in TEM as expected, as the former display the hydrodynamic radius value.

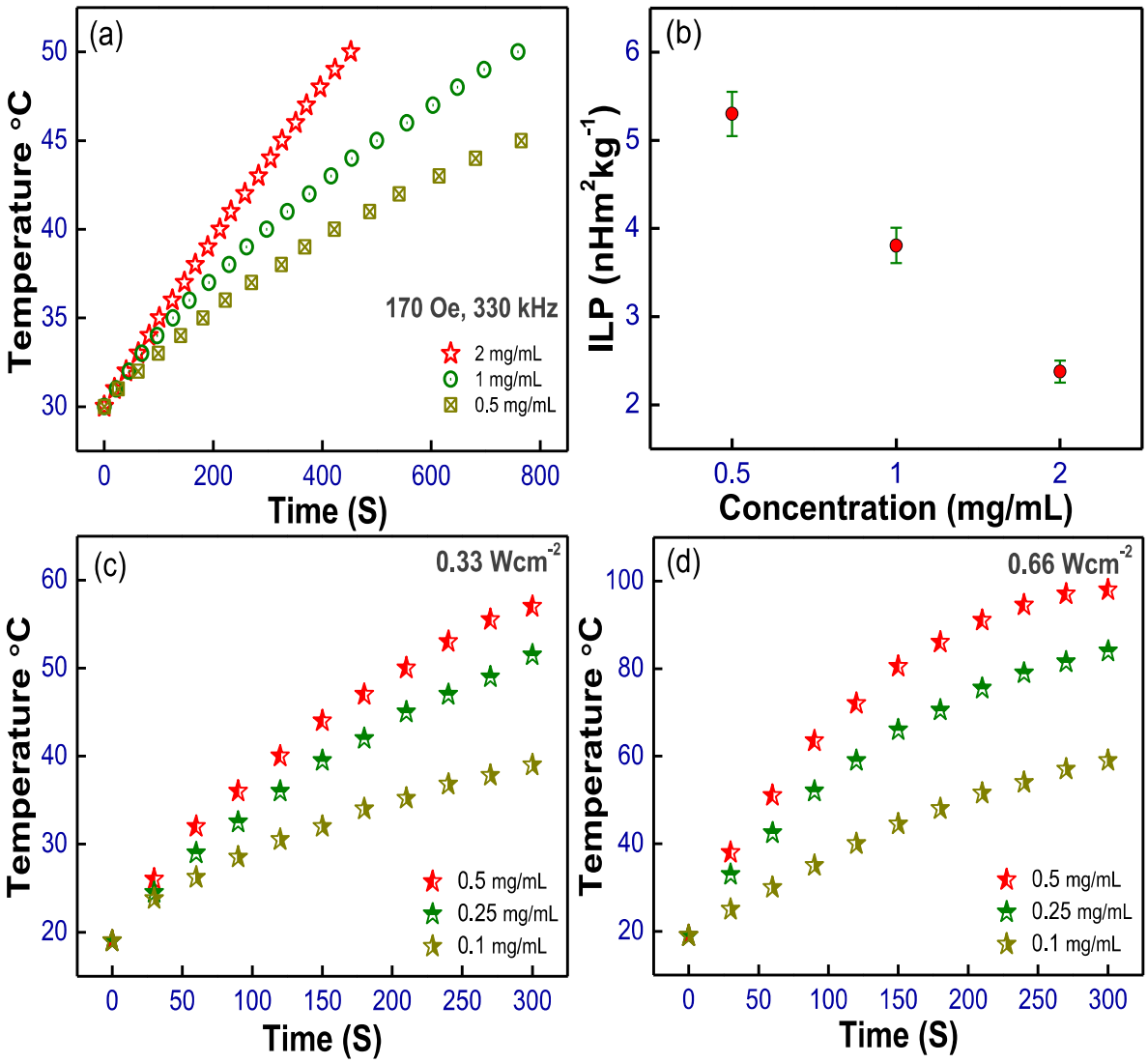


*Figure 5. 11: (a) Concentration dependent temperature rise profile with time of aqueous ferrofluids at 170 Oe and 330 kHz, (b) corresponding ILP values of the ferrofluids, and concentration dependent heating behaviour of aqueous suspensions when exposed to NIR laser of power density (c) 0.33 $Wcm^{-2}$ and (d) 0.66 $Wcm^{-2}$.*

*Figure 5.11a* illustrates the concentration-dependent temperature increase profile of aqueous ferrofluids of mesoporous $Fe_3O_4$ at an AMF of amplitude 170 Oe and frequency 330 kHz. The ferrofluids demonstrated a continuous rise in temperature till the AMF was applied. The therapeutic temperature of ~42 °C was achieved even at the concentration of 0.5 mg/mL after 541 s of AMF exposure. The time taken to attain this therapeutic temperature

reduced with increasing the concentration of ferrofluid. For example, at concentration of 1 and 2 mg/mL the therapeutic temperature was attained after 376 and 258 s of AMF exposure, respectively.

*Figure 5.11b* represents the corresponding concentration-dependent ILP values of the ferrofluids. A high ILP value of ~5.30 ± 0.25 $nHm^2kg^{-1}$ was obtained during MFH, at an AMF of amplitude 170 Oe and frequency 330 kHz, for the aqueous ferrofluid of concentration 0.5 mg/mL. At same AMF γ-$Fe_2O_3$ and $MnFe_2O_4$ nanoflowers displayed an ILP value of 15.21 ±0.34 and 5.70 ± 0.085 $nHm2kg^{-1}$, respectively. As observed, the ILP valued enhanced at lower concentrations. The reason for such an observation could be due to an increase in anisotropy energy at higher concentrations due to enhanced dipole-dipole interactions leading to the increased agglomeration [102], [103]. Also, a chain-like formation of nanoparticles was perceived in TEM. It has been observed that chain formation could enhance or diminish the heating efficiency depending on the length of such assembly [46]. Of course, the increased length would add to the total effective anisotropy, thus decreasing the efficacy at the same AMF. As the increased effective anisotropy could restrict the magnetization reversal (or magnetic moment rotation) in field direction and thus a decrease in heating would be observed. Nevertheless, one could expect enhanced heating at higher amplitude AMF, as it would be sufficient to align the magnetic moment in the field direction. In general, the maximum in heating could be observed with an AMF of amplitude close to the anisotropy field of the material [80]. Also, the role of frequency of AMF could not be alleviated in the heating behaviour, which increases with increased frequency but up to a specific limit [46], [81]. Since the usable combination of amplitude and frequency of the

AMF is limited by the physiological constraints, a higher field and frequency could not be utilized.

*Figure 5.11c* and 5.*11d* show the concentration-dependent temperature elevation prolife of the aqueous suspension of the sample after irradiation with NIR laser (808 nm) of power density 0.33 and 0.66 $Wcm^{-2}$, respectively. As evident, the temperature rise was affected by the concentration of the aqueous suspension and NIR laser power density. On exposure with the NIR radiation of 0.66 $Wcm^{-2}$ for 5 minutes, the temperature reached ~98, 84 and 59 °C (initial temperature was 19 °C) of the aqueous suspension of concentration 0.5, 0.25 and 0.1 mg/mL, respectively. The DD water at the identical situation exhibited a temperature rise of ~ 2°C, confirming that the nanoparticles were principally liable for the heating. Lowering the power density to 0.33 $Wcm^{-2}$ resulted in a drop in the temperature rise after the same exposure period. The aqueous suspension of concentration 0.5, 0.25 and 0.1 mg/mL reached the temperature of ~57, 51.5 and 39 °C, respectively, after 5 min of exposure. The DD water at this power density showed no prominent temperature increment (< 1 °C). The photo-thermal behaviour of the mesoporous $Fe_3O_4$ could better be evaluated from the photoluminescence and absorption spectra, as a limited radiative emission and significant absorption near the NIR region are the requisites for better photo-thermal conversion.

*Figure 5.12a* shows the PL excitation spectrum of mesoporous $Fe_3O_4$ while monitoring the emission at 550 nm. The spectrum displayed a peak around 245 nm. $Fe_3O_4$ has an inverse spinel structure with oxygen ion in face centered cubic (FCC) array and equal distribution of $Fe^{3+}$ at tetrahedral and octahedral and $Fe^{2+}$ at octahedral sites [198]. The excitation band at 245 nm with the energy of ~ 5.0 eV is ascribed to electronic transition from the O(2p) valence band to the empty Fe(4s) [160]. Under the influence of the octahedral

and tetrahedral crystalline field, there is a further separation of O-2p from its crystal field site by about ~ 1eV [140]. The PL emission band at around 550 nm (*Figure 5.12b*) is ascribed to radiative transition of electrons from $e_g \rightarrow t_{2g}$ on the octahedral sites [140], [186]. The color coordinate diagram shows emission of green color light by mesoporous iron oxide under UV irradiation (*Figure 5.13a*). In the mesoporous $Fe_3O_4$, along with the 550 nm green band, an intense NIR band was observed around 900 nm with a very high photon count (*Figure 5.12c*). This band could be ascribed to electron traps on the tetrahedral site, which are associated with the oxygen vacancies [140], [186]. But the peculiar shape is missing due to the limitation of the instrument which is blind beyond 900 nm owing to the PMT detector currently existing in the fluorimeter. One more band at 690 nm was present in the $Fe_3O_4$ nanoparticle due to

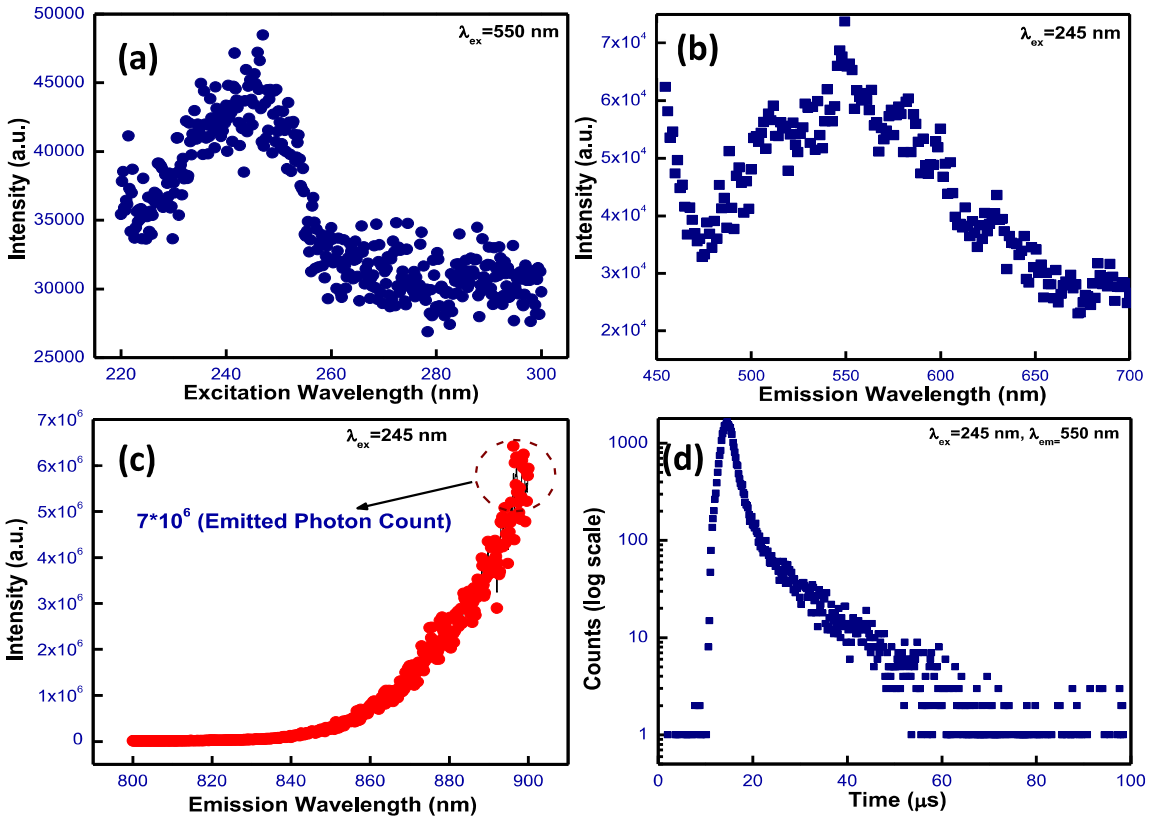


*Figure 5. 12: (a) PL excitation, (b) PL emission (Visible Region), (c) PL emission (NIR region) and (d) luminescence decay profile of mesoporous $Fe_3O_4$ nanoparticles.*

the recombination of trapped electrons on the octahedral site to O-2p [186]. The electrons can non-radiatively transfer to these defect sites by releasing the thermal energy, causing the temperature rise of the system [156]. Thus, an intense NIR peak around 900 nm is one reason for the excellent photo-thermal behaviour of the nano-crystalline mesoporous $Fe_3O_4$.

Luminescence lifetime spectroscopy under 245 nm excitation and monitoring the emission of 550 nm light displayed monoexponential decay behaviour with a lifetime value of 8.96 µs (*Figure 5.12d*). It is a typical lifetime of oxygen vacancy in oxide lattice.[54] This again supports our analogy that 900 nm emissions have a contribution from oxygen vacancies. The mechanism of visible PL in the green region around 550 nm and a very intense NIR band at around 900 nm in our mesoporous $Fe_3O_4$ has been shown schematically in *Figure 5.13b*. The basis of this scheme has been formulated based on the model suggested by *Sadet et al.*[156].

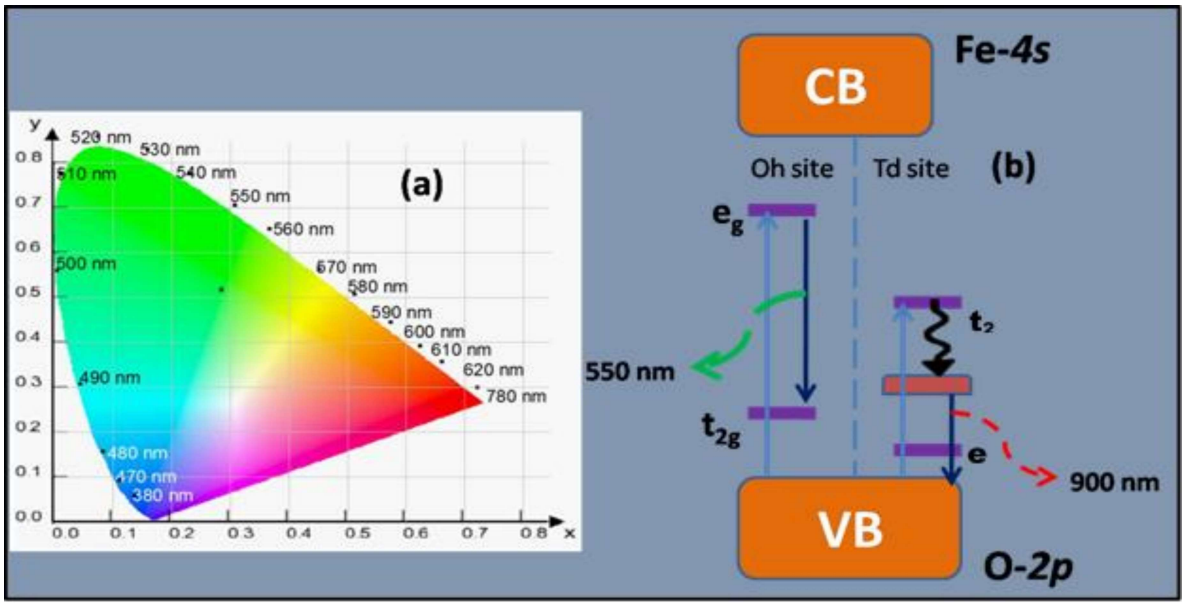


*Figure 5. 13: (a) Visible region Color Index Diagram and (b) schematic showing mechanism of visible and NIR PL peak in mesoporous $Fe_3O_4$ nanoparticles.*

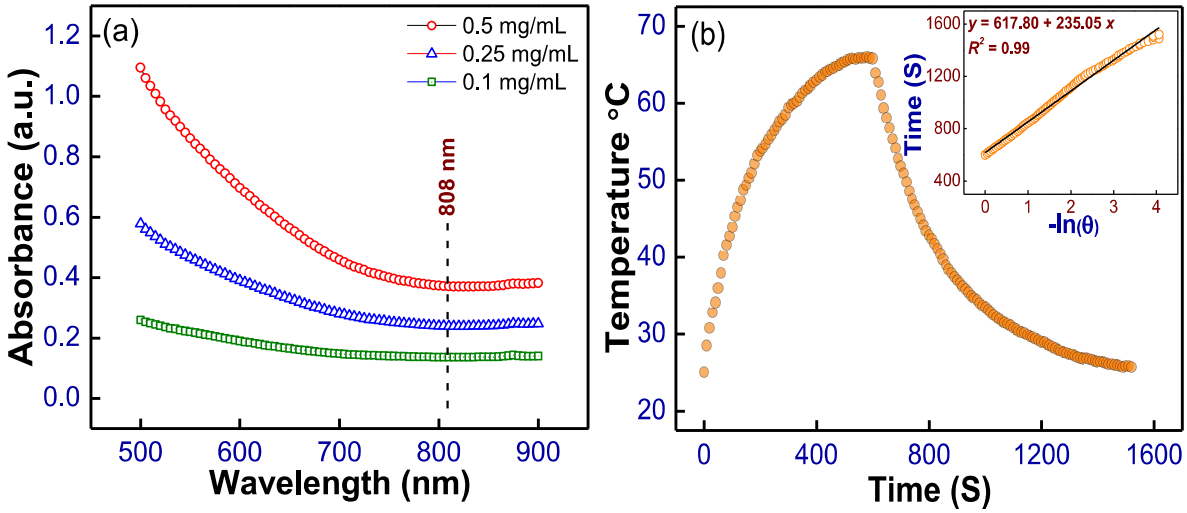


*Figure 5.14: (a) Concentration dependent UV-vis absorption spectra, and (b) heating and cooling curve for 0.5 mg/mL aqueous suspension with 808 nm laser irradiation of 0.33 $Wcm^{-2}$ power density.*

The curves in *Figure 5.14a* represent the concentration-dependent absorption behaviour of the aqueous suspensions of mesoporous $Fe_3O_4$ measured over a wavelength span of 500 to 900 nm. The suspensions exhibited finite absorbance over the entire span, which decreased with increasing wavelength. A finite absorbance near the NIR region, which was 0.37, 0.24 and 0.14 at the concentration of 0.5, 0.25 and 0.1 mg/mL, respectively, were observed for the suspension. *Figure 5.14b* shows the time-dependent heating and cooling curve of the aqueous suspension of concentration 0.5 mg/mL after exposing it to 808 nm NIR of 0.33 $Wcm^{-2}$ power density. A decay time of ~ 235 s was calculated from the cooling curve and is shown as the inset of *Figure 5.14b*. The corresponding *hA* value was calculated to be 8.93 W/°C. The energy input calculation due to the heat generated by the solvent is given elsewhere, and its value was obtained to be 3.56 mW at the power density of 0.33 $Wcm^{-2}$.[22] A photo-thermal conversion efficiency of ~61 % was obtained for the mesoporous $Fe_3O_4$ using relation 2.3 (chapter 2). In the previous work, this efficiency was found to be ~70 % and 63 % for γ-$Fe_2O_3$ and $MnFe_2O_4$ nanoflowers, respectively. Though, the temperature

raised is higher in the present case, the comparatively lower efficiency is due to the relatively higher absorbance of mesoporous $Fe_3O_4$ at 808 nm. Recently, *Bertuit et al.* [199] recognized higher photo-thermal heating behaviour of $Fe_3O_4$ nanoflowers than the γ-$Fe_2O_3$ nanoflowers under similar experimental conditions. For IONPs with different coatings, *Sadat et al.*[140] had observed '$\eta$' values ranging from ~16-76 %, equivalent to that of mesoporous $Fe_3O_4$ obtained through the solvothermal process.

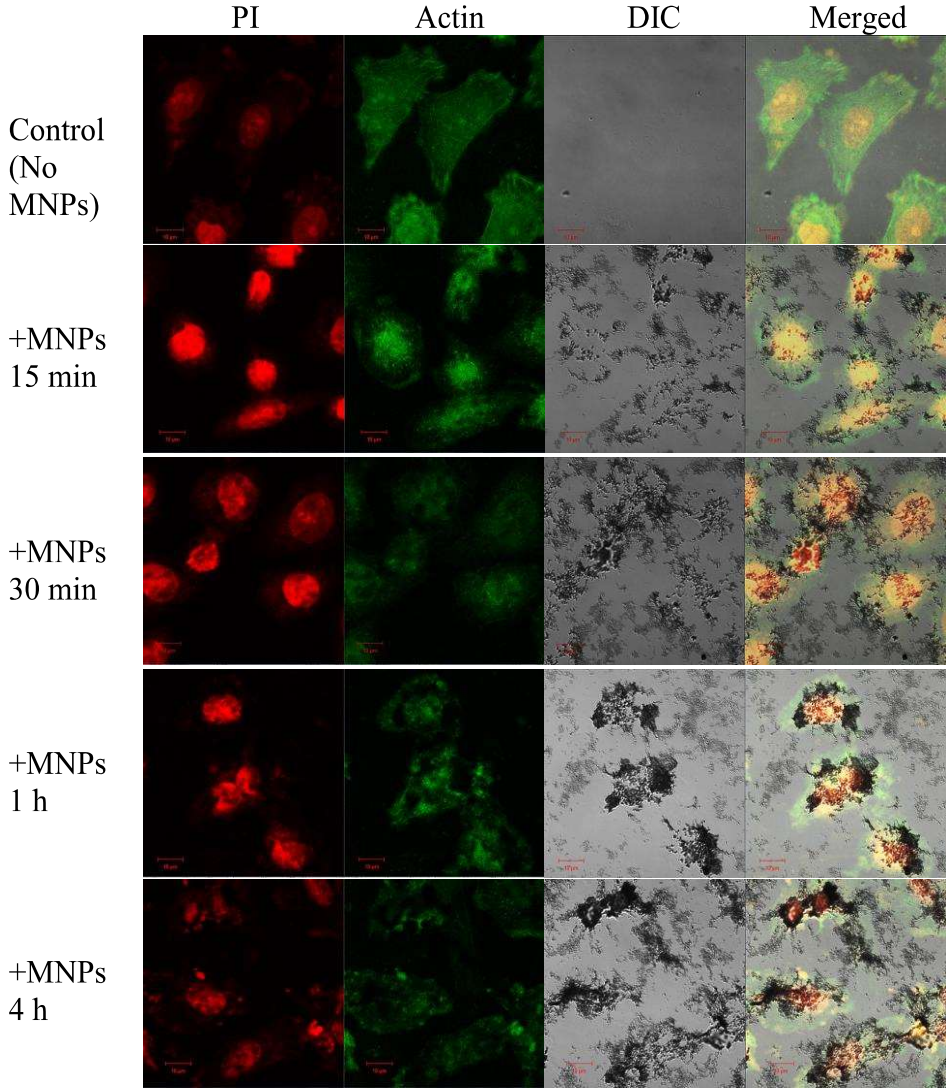


*Figure 5. 15: Confocal microscopy images showing SiHa cells stained with phalloidin (green, for actin in cytoplasm) and propidium iodide (red, for nucleus) with and without MNPs incubation at different time intervals.*

Confocal images (*Figure 5.15*) show that the MNPs start to attach to the SiHa cells as early as 15 min of incubation. It can be observed that at the MNPs locus the green actin signal appears dark which suggests that the particles are internalized and reduced visibility of actin stained with fluorescent labeled phalloidin. A significant amount of MNPs' accumulation was itself observed after 1 h of incubation which further increased with incubation duration. Thus, before PTT experiments the cells were incubated with magnetic material for 1 h.

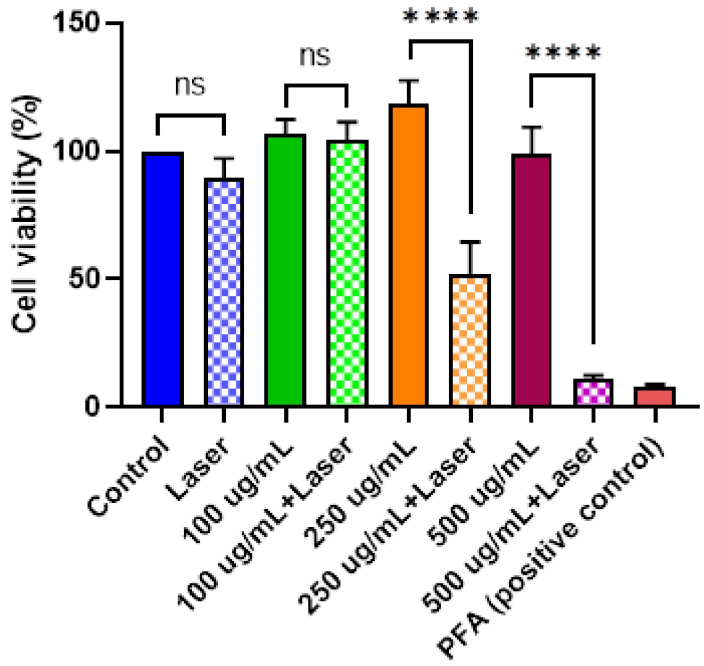


*Figure 5. 16: MTT assays of SiHa cells with and without MNPs and PTT (laser treatment); ns: not significant, ****:$p \leq 0.0001$.*

SiHa cells viability was assessed by MTT assay after concentration dependent PTT. The MTT assay confirmed that there was no induced toxicity to SiHa cells after 1 h incubation with MNPs alone. Indeed, a slight enhancement in viability was observed up to 0.25 mg/mL of MNPs (*Figure 5.16*). Also the laser exposure (5 min duration) to the cells, which were not incubated with MNPs, did not induced any significant toxicity. However,

after PTT with $Fe_3O_4$ MNPs of concentrations 0.25 and 0.5 mg/mL with 808 nm laser of 0.66 $Wcm^{-2}$ power density for a duration of 5 min, the cell viability was significantly reduced (compared by one-way ANOVA test) to ~ 52% and 11% respectively. Although therapeutic

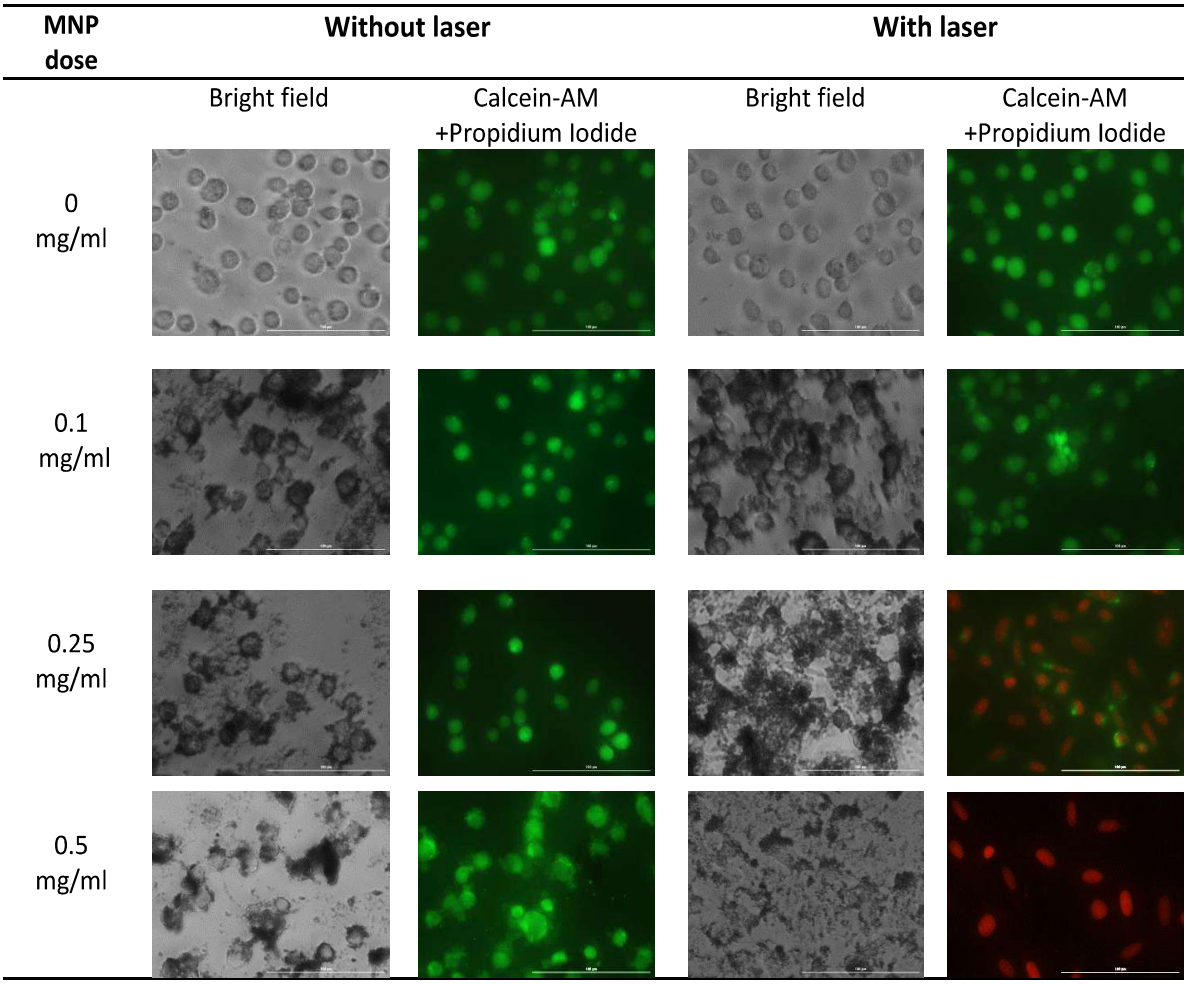


*Figure 5. 17: Fluorescence microscopy images showing SiHa cells stained with Calcine-AM (green) and propidium iodide (red, for nucleus) after PTT.*

temperature was even achieved with 0.1 mg/mL of MNPs under similar experimental condition, it failed to induce any toxicity to the SiHa cells, demanding a higher concentration or longer treatment duration. From the fluorescence microscopy the cell damage was apparent as red signal of increased propidium iodide signal, when treated with 0.25 and 0.5

mg/mL MNPs after PTT (*Figure 5.17*). The disruption of the cells is also visible in bright field image and a substantial effect could be produced within 5 min through one-time treatment only.

### 5.3. Conclusion

The $Fe_3O_4$ mesoporous nanoparticles have successfully synthesized, as observed by TEM, using a facile solvothermal process. The XRD pattern confirmed the formation of single-phase material having a non-stoichiometric structure as identified by Mössbauer spectroscopy. The material displayed an early saturation behaviour having high saturation magnetization value of ~83 emu/g at room temperature, which indicates to the synthesis of high quality nanoparticles. A high ILP value of ~5.30 ± 0.25 $nHm^2kg^{-1}$ was obtained during MFH, at an AMF of amplitude 170 Oe and frequency 330 kHz, for the aqueous ferrofluid of concentration 0.5 mg/mL. The ILP value decreased on increasing the concentration of the ferrofluid due to the effect of enhanced dipolar effect at higher concentrations. The material showed extraordinary heating behaviour under NIR (808 nm) irradiation of 0.33 $Wcm^{-2}$ power density. The intense NIR photo-counts observed in NIR PL experiments, due to the trapped electrons in the tetrahedral site, is the primary reason for their excellent photo-thermal performance. The aqueous suspension of the mesoporous nanoparticles showed good absorbance near the NIR region and photo-thermal conversion efficiency of ~61%. Moreover, under NIR irradiation, the therapeutic temperature of ~42-46 °C was achievable even at a low concentration of 0.1 mg/mL aqueous suspension. The in-vitro studies showed that the mesoporous $Fe_3O_4$ nanoparticles could easily internalize in the cells and a high rate of cells death was noticed during PTT even at a concentration as low as 0.25 mg/mL for an exposure time of only 5 min. The report backs the mesoporous $Fe_3O_4$ nanoparticles as an

efficient magnetic- and photo-thermal agent. Though, *in-vivo* studies are essential before any commercial use.